AWG Model Validation Through Measurement of Fabricated Devices

Pascual Muñoz, *Student Member, IEEE*, Daniel Pastor, *Member, IEEE*,
José Capmany, *Senior Member, IEEE, Fellow, OSA*, Daniel Ortega, Antoine Pujol, and
Jim R. Bonar

***Abstract*—In this paper, the validation of a previously published arrayed-waveguide grating (AWG) model is presented, using measures of fabricated devices. The measured spectrum, dispersion, and loss, along with Fourier spectroscopy (FS) measurements of the array errors, are used to verify the numerical simulations and analytical derivations for a Gaussian AWG device. The verified model is then used to investigate the relationship between the different fabrication errors and their impact on the response of flat-top AWG devices. Several conclusions are presented about the accuracy on the use of FS measurements in this modeling, since some discrepancies between the FS measurements and simulations are found and discussed and their motivations identified. Moreover, the ability and flexibility of this model to distinguish and clarify the source of each degradation in the performance of flat-top AWGs is proven.**

***Index Terms*—Arrayed-waveguide gratings (AWGs), Fourier spectroscopy, modeling, optical planar waveguide components, software performance, software reliability, software testing.**

I. INTRODUCTION

SINCE the first report of an arrayed-waveguide grating (AWG) device [1], a significant amount of effort and interest have been concentrated in this device due to its special frequency–space properties, which have been exploited in a wide range of applications, such as optical signal processing [2], [3], wavelength-division multiplexing/demultiplexing [4], fiber-ring lasers [5], wavelength interleavers [6], and wavelength routers [7], to name a few. The interest has not only been directed to the applications of the device, but also to the modeling of its properties and behavior, in order to tailor its response. Several models exist in the literature: the one by Dragone [8], [9], which borrows principles from the anthena theory; the formulation by Takahashi *et al.* in [4] and [7], reviewed later on by Smit in [10], which is based in the grating equation from the planar spectrograph theory [11]; the model proposed by Parker and Walker in [12], based in the Fresnel–Kirchhoff diffraction integral; and the model presented in the authors' previous work [13], based in Fourier optics. All these models have been used to design AWG devices; however, to the best of the authors' knowledge, none of them has been validated in the following terms: the reproduction of relevant response magnitudes (transmittance-shape, bandwidth, adjacent channel crosstalk, crosstalk floor, in-band dispersion) and internal [amplitude and phase of the field distribution in the arrayed waveguides (AWs)] of previously fabricated devices. Moreover, part of the previously mentioned models are based in geometrical assumptions [4], [7], [10], and they do not provide an end expression for the field transfer function of the AWG. Other models [8], [9], [12] give this end expression, but the formulation nature does not allow for the piecewise investigation of the AWG, since an end-to-end expression is produced, in terms of the summation of the contributions of the AWs. The model described in the previous work [13] has both characteristics: a field transfer function expression for the AWG that is developed piecewise. Hence, this model is suitable to investigate the relationship between the fabrication imperfections and their associated response degradations.

This objective would not be possible without validating first the model to be used. To do so, work has been carried in collaboration with an AWG manufacturer, which was Alcatel Optronics UK (AOUK, formerly Kymata, Ltd., and now Avanex). The paper is structured as follows. First, Section II deals with a brief review and description of the model to be used and the data provided by AOUK. The validation of the model is divided into two steps in the paper. First, the modeling of the SCs using the Fresnel diffraction integral is checked in Section III. Once these parts of the model are validated, the full field transfer response given by the model is investigated in Sections IV and V, for Gaussian (the transmittance resembles a Gaussian function) and flat-top (the transmittance is a box-like function) AWG devices, respectively, where the rest of the parts of the model, which will be introduced later, are validated. Finally, the conclusions are presented in Section VI.

II. MODEL DESCRIPTION AND INPUT DATA FOR VALIDATION

The model to validate with the measurements provided by AOUK is described in [13]. As a summary, the model is derived piecewise by dividing the calculation of the final AWG field transfer function into four parts, corresponding to the different parts that can be found in a $1 \times N_o$ AWG, which is depicted in Fig. 1. First, the diffraction from the input waveguide (IW) through the first slab coupler (SC) is performed by solving the

---

Manuscript received December 4, 2003; revised May 28, 2004. This work was supported in part by the European Commission through the Information Society Technology (IST) programs under IST-2001-37435-LABELS and IST-2001-32786-NEFERTITI and by the Spanish Comisión Interministerial de Ciencia y Tecnología (CICYT) funding under Project TIC 2002-04344-PROFECIA.

P. Muñoz, D. Pastor, and J. Capmany are with the Optical Communications Group and IMCO2 Research Institute, Departamento de Comunicaciones, Universidad Politécnica de Valencia, 46022 Valencia, Spain (e-mail: pascual@ieee.org).

D. Ortega and A. Pujol were with Alcatel Optronics UK, Livingston EH54 8SF, U.K.

J. R. Bonar is with Avanex, Livingston EH54 8SF, U.K. (e-mail: jim_bonar@avanex.com).

Digital Object Identifier 10.1109/JLT.2004.833275

Fresnel diffraction integral [14]. This is different from [13], where Fourier transforms were used instead as an approximation to derive closed expressions. However, the numerical calculations are exact using the Fresnel integral, although the calculation time is increased. The solution of the Fresnel integral is the field distribution, amplitude and phase, before the AWs. This field distribution excites the fundamental mode in each one of the AWs, whose length is changed incrementally by a fixed amount between consecutive waveguides, providing the basic frequency-dependent focusing property of the AWG [1]. Therefore, the phase change that each waveguide undergoes is different, and this is modeled by a complex exponential term [13]. The third calculation step in the AWG model is the diffraction from the AWs through the second SC, as can be seen in Fig. 1, which is also performed by a second Fresnel integral. Note that the geometrical conditions are different for the first and second SC, and although the Fresnel integral is the same, the particularization and numerical calculations are different for the two slabs. The diffraction of the second slab gives the field distribution before the output waveguides (OWs). Finally, to calculate the amount of energy coupled to the OWs, the overlap integral between the mentioned diffraction pattern and the OW fundamental mode must be solved to yield the AWG field transfer function. The mathematical equations are extensively described in [13].

The input data provided by AOUK are the following:[1]

1) AWG design parameters for Gaussian (AWG-G) and flat-top (AWG-F) devices, which include slab length L_f, slab dispersion $n_s(f)$, AW spacing d_w, number of AWs N, design frequency f_0, AW length increment $\Delta(f_0)$, grating order m, number of channels N_o, OWs location angles $\alpha_{\mathrm{ow},k}$, and OW target frequencies (centers of the passing bands) $f_{\mathrm{ow},k}$ $k \in [1, N_o]$;
2) waveguides, tapers, and horns modes, core and cladding indexes n_{co} and n_{cl}, and waveguide dispersion $n_c(f)$;
3) end-to-end measured AWs field amplitude (A_k) and phase (ϵ_k) distribution;
4) transmission spectra, bandwidth for 0.5-, 1, 3-, and 20-dB points (AWG-G and AWG-F) and in-band dispersion (AWG-G).

In other literature, as for instance [15], the validation carried so far involves the calculation of the transmittance defined as

$$T(f) = \left| \sum_{k=0}^{N-1} A_k e^{i\epsilon_k} e^{i2\pi \frac{c}{f} n_c(f) \Delta L} \right|^2 \tag{1}$$

where A_k and ϵ_k are measured using Fourier spectroscopy (FS) [15]. The measurement method is based on optical low coherence interference, in which the AWG is seen as a 1 × 1 linear circuit placed in one arm of an interferometer, as depicted in Fig. 2. The distance between the prism and the reflector is changed mechanically. When the optical length in both arms of the interferometer is matched, a fringe is produced in the waveform recorder. The optical length is different for each AW; thus, it is possible to measure each AW independently [15]. The Fourier transform of the fringe allows us to obtain the amplitude and phase for each AW. This is an indirect method to measure the AW field, amplitude, and phase, distribution, since it is not possible to measure directly this distribution once the AWG has been fabricated. As this is an end-to-end measure, it is reasonable to think that it may include other effects from the second SC and the overlap with the OW. Under these conditions, (1) yields a perfect representation of the transmittance, since the coefficients A_k and ϵ_k are measured end to end, and therefore they include the contributions of all the parts of the device to the OW. These measurements depend both on the frequency and on the OW considered. In fact, the errors can be due to different causes, for instance, truncation of the field distribution at the input side of the AWs and coupling in the AWs, which can be avoided to some extent at the design stage, or unavoidable fabrication errors due to the material un-uniformity or finite photomask resolution [16]. The design of the devices used for this paper avoids truncation and coupling in the array, and therefore only fabrication errors are present.

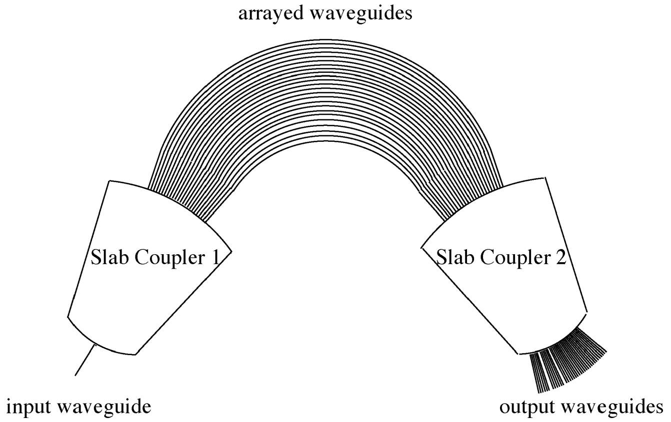

Fig. 1. $1 \times N_o$ AWG layout, divided into four parts for calculations: the IWs + first SC, the AWs, the second SC, and the OWs.

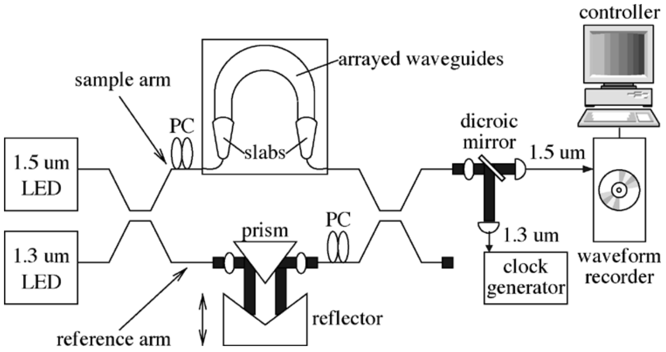

Fig. 2. FS setup for the measurement of the AW amplitude and phase distributions.

In the next sections, the validation of the model follows. In Section III, the SC modeling is verified. This can be done separately from the rest of the model, under certain assumptions that follow. It involves the numerical resolution of the Fresnel integral and the comparison of the results with the AW field, amplitude and phase, distribution measured by FS. In Section IV, the two remaining parts of the model are tested for an AWG-G.

---

[1] Within the paper, not all the design values are shown, since they are sensitive information belonging to AOUK.

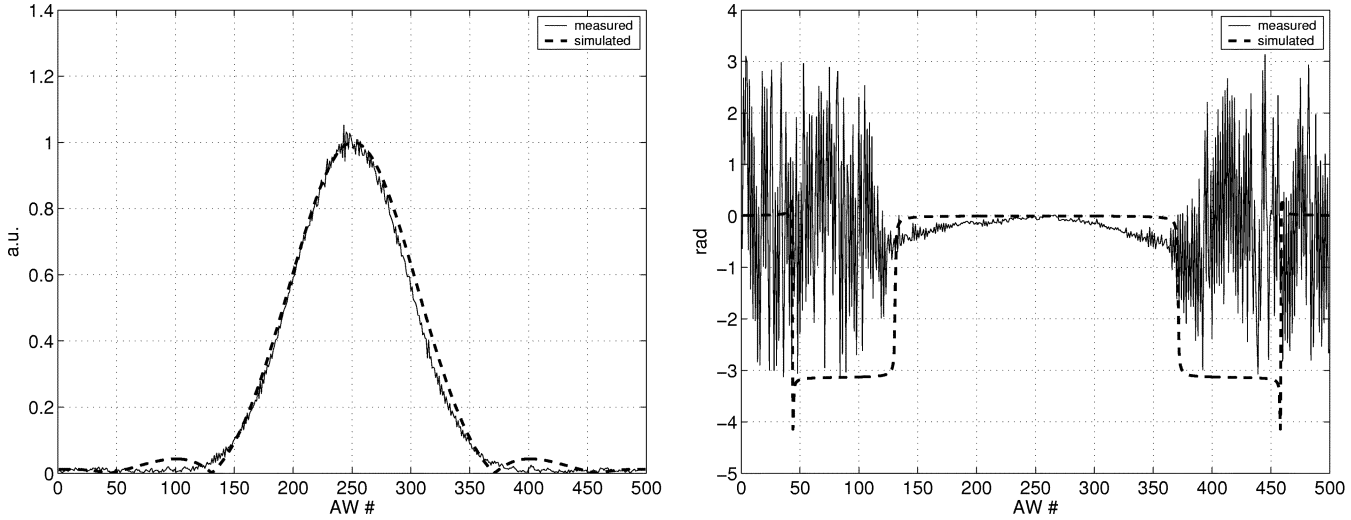

(a) Amplitude (b) Phase

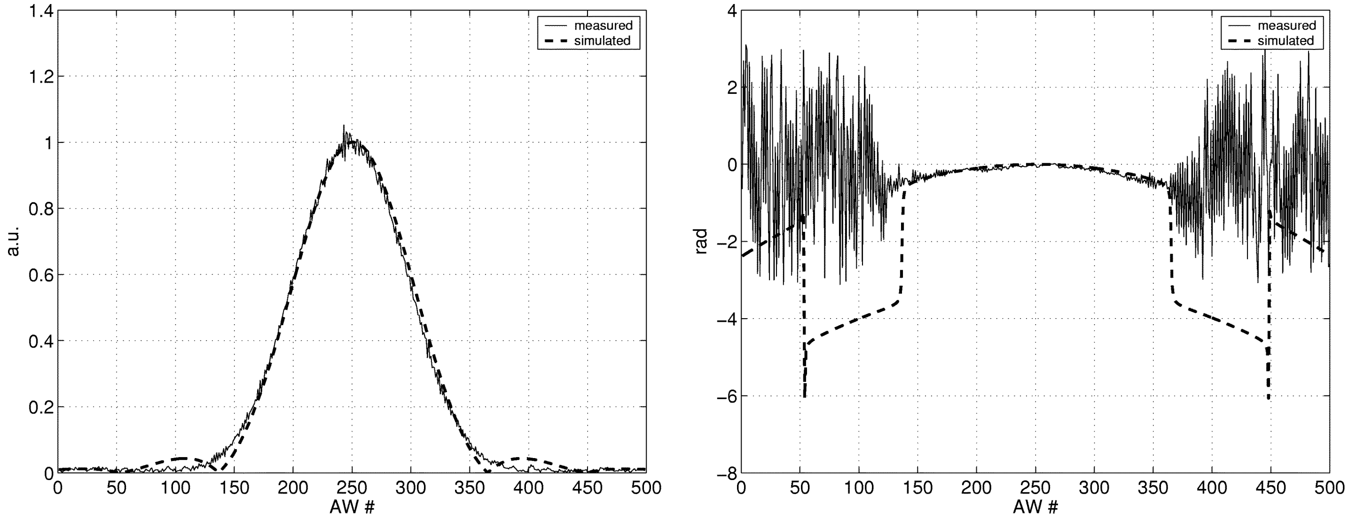

(c) Amplitude (slab defocused) (d) Phase (slab defocused)

Fig. 3. AW amplitude and phase measured (solid line) and simulated (dashed line) distributions under (a), (b) ideal and (c), (d) defocused situations of SC 1.

These parts are the focusing of the AWs and the OW overlap integrals. The verification is carried out by combining these parts with the previously checked SC modeling and comparing the simulated and measured spectrums and dispersion. Only after the model has been validated for Gaussian devices is the investigation for flat-top devices initiated in Section V.

III. SLAB COUPLER MODELING VERIFICATION

As mentioned previously, to calculate the field distribution at the end of each SC, the Fresnel diffraction integral must be solved numerically. The next two subsections deal with the verification of the first and second SC, respectively.

A. Input Slab Coupler Verification

To check the implementation of the Fresnel integral for the first SC, the following inputs are provided to the model:

1) IW taper W_i and spatial modal field $b_i(x_0)$, where x_0 is the IW coordinate;
2) first SC length L_f;
3) slab refractive index $n_s = 1.430\,26$;
4) AW spacing d_w;
5) AW number $N = 499$;
6) design frequency $f_0 = 193.95$ THz.

The output from the model is the field distribution for the AWs $B_i(x_1)$, which is retrieved numerically, where x_1 is the coordinate at the end of the first SC [13]. The obtained field distribution is compared with the measurements in Fig. 3(a) and (b). First, the amplitude obtained by simulation exhibits sidelobes, as can be seen from Fig. 3(a) from waveguide numbers 30 to 124 and 378 to 472. This fact is consistent with the following analytical derivation. The modes in the IW are found by solving the Maxwell's equation with the particular boundary conditions of the square waveguide [17], yielding

$$b_i(x_0)=\begin{cases}\frac{1}{\sqrt{P_e}}\cos(h_1x_0), & |x_0|\leq\frac{W_i}{2}\\ \frac{1}{\sqrt{P_e}}\cos\left(\frac{h_1W_i}{2}\right)\exp\left\{-h_2\left(|x_0|-\frac{W_i}{2}\right)\right\}, & |x_0|\geq\frac{W_i}{2}\end{cases} \quad (2)$$

which is a cosine in the core and a decaying exponential in the cladding, where W_i is the waveguide width, h_1 and h_2 are the solutions of the transverse-electric (TE) mode eigenvalue equation, and P_e is a power normalization coefficient [17]. It is possible to calculate the diffraction analytically using the Fourier transform and rewriting the real mode from (2) as

$$b_i(x_0)=\prod\left(\frac{x_0}{W_i}\right)\cos(h_1x_0)+\mathrm{rect}\left(x_0-\frac{W_i}{2}\right)e^{-h_2\left(x_0-\frac{W_i}{2}\right)} +\mathrm{rect}\left(-x_0-\frac{W_i}{2}\right)e^{+h_2\left(x_0+\frac{W_i}{2}\right)} \qquad (3)$$

where $\prod(x)$ is 1 for $|x| \leq 1/2$ and 0 elsewhere, and rect(x) is 1 for $x > 0$ and 0 otherwise. Then, using the Fourier transform, $\mathcal{FT}\{\}$, instead of the Fresnel integral, as in [13]

$$B_i(u) = \frac{W_i}{2}\mathrm{sinc}(W_iu) \star \left[\delta\left(u+\frac{h_1}{2\pi}\right)+\delta\left(u-\frac{h_1}{2\pi}\right)\right] +\mathcal{FT}\{\mathrm{exponentials}\} \qquad (4)$$

with $u = x_1/\alpha$ and α given by [13], as follows:

$$\alpha = \frac{cL_f}{n_s f_0}. \qquad (5)$$

The values of h_1, h_2, and α for the given inputs make the deltas to be at $u = 0$. Hence, the convolution operator leaves the sinc function also at $u = 0$. Note that the zeros of the sinc function Δx_1 are located at

$$\Delta x_1 = \alpha\Delta u = \frac{\alpha}{W_i}. \qquad (6)$$

Therefore, the truncation of the cosine function in (3) will yield a sinc-like field distribution over the AW interface, with zeros related to the IW width. Since $\Delta x_1 = 94d_w$, with the design parameters given previously, we obtain

$$\frac{cL_f}{n_s f_0 94 d_w} \simeq W_i. \qquad (7)$$

This is an important difference when using real modes instead of the Gaussian approximation in [13] and the first of the discrepancies we found between the simulation and the FS measurements, since the latter does not have these sidelobes, as can be seen in Fig. 3(a). The sidelobes are approximately 28 dB below the maximum, and they are located also in the AWs for which the phase distribution is not retrieved with the FS measurement method, as can be seen in Fig. 3(b). These two facts lead to the conclusion that the FS measurement method, which is interferometric, may conceal the sidelobes. This has been also reported by Takada *et al.* in [15]. In that paper, the authors show that it is not possible to measure the amplitude and phase distribution for all the AWs since the measurement is limited by electrical noise and that only for the waveguides where the field amplitude is high, i.e., the central AWs, the measurement is valid, with measurement error increasing as one departs from the central waveguides. Recently, some numerical processing techniques have been reported to enhance measurement accuracy [18]. Moreover, the FS is an end-to-end measurement method, and the simulator is providing the AW amplitude in a direct way, without being affected by the second SC or the OW overlap integral,or the limitations of the FS method. Therefore, if FS measurements are used for comparison with the Fresnel integral in the SCs, only the central waveguides should be compared, as for instance waveguides 150–350 in Fig. 3.

Concerning the comparison of the simulated and measured phase distribution for the AWs [Fig. 3(b)], note that the measured phase is slightly curved, while the simulated is perfectly straight. We considered this can be due to second-order phase errors introduced in the array or the slabs during the fabrication of the devices. The second-order phase errors are equivalent to defocusing of the AWG. It is possible to model defocusing by altering the slab length L_f while maintaining the waveguide geometrical arrangement. Although we did not develop an analytical expression to evaluate the defocusing through the model presented in [13], it is still possible to explore its effects by numerical simulations. Fig. 3(c) and (d) corresponds to the situation where the SC 1 is defocused by -18 μm. This value was obtained empirically, after some simulation iterations, without following any optimization procedure. From the figures, it can be observed that the amplitude and phase distribution are best matched in this case and that the sidelobes are still present.

Therefore, with the results and derivation presented, we can conclude that the model reproduces the first SC, and that it can be used to describe additional effects as defocusing.

B. Output Slab Coupler

To cross-check the second SC, the one-to-one imaging nature of the AWG must be taken into account: if the AWG is designed symmetrically, i.e., with the same SC length and AW spacing at both sides of the device, the field pattern produced at the output of the second SC must be very similar to the IW mode field. The reasoning is valid as long as the number of AWs N is properly chosen, in such a way that the truncation of the field distribution in the AWs is kept low. The test performed in this subsection consists of the propagation of the field from the IW $b_i(x_0)$ to the output plane of the AWG, for $f = f_0$.[2] This must yield a field distribution in the output plane x_3 before the OWs, named $f_3(x_3)$, similar to that in the IW, since the AWG configuration with two identical SCs is a one-to-one imaging device, as mentioned previously. The phase shifts are skipped since they are only responsible, in a first approximation, for the movement of the image $f_3(x_3)$ (lens pattern) along the output focusing plane x_3. Therefore, the calculation performed can be roughly summarized analytically as

$$b_i(x_0) \rightarrow^{\mathrm{FT}} B_i(x_1) \rightarrow^{\mathrm{FT}} f_3(x_3) = b_i(-x_3) \qquad (8)$$

where FT means Fourier transform, thereby ending with a reversed image of the input due to the two consecutive direct Fourier transforms [19]. In the numerical calculations, the Fourier transform is replaced by the Fresnel integral, as in the last subsection. After this discussion, the inputs to the modeling tool are as follows:

1) IW taper W_i spatial modal field $b_i(x_0)$, where x_0 is the IW coordinate;
2) SC 1 and SC 2 length L_f;
3) slab refractive index $n_s = 1.430\,26$;

---

[2] This is equivalent to skipping the phase shifts due to the AWs (see [13]).

4) AW spacing d_w;
5) AW number $N = 499$;
6) design frequency $f_0 = 193.95$ THz.

Then, the two slabs are simulated consecutively. For a frequency $f = f_0$, this should yield the input image focused at $x_3 = 0$, i.e., the center of the output plane [13]. The results are presented in Fig. 4. As expected, the input image is reproduced over the output plane, since the output pattern and the IW mode are identical, as seen in the figure. Therefore, it is possible to conclude that the second SC is being modeled properly.

Hence, up to this point, the modeling of the SCs using the Fresnel integral has been successfully cross-checked with the FS measurements, and moreover, the discrepancies found have been analyzed and discussed analytically as well. There are still two parts of the modeling that have not been verified: the frequency-dependent focusing through the AWs and the overlap integral of the lens pattern $f_3(x_3)$ with the OW mode field. These two characteristics are checked in the next section for a Gaussian AWG design.

IV. FULL GAUSSIAN AWG MODEL VALIDATION

The full model test consists on the end-to-end simulation of the AWG, which yields the field transfer function for a given IW–OW pair. In linear systems theory [20], the transfer function characterizes time-invariant systems, as the AWG. In our case, we will name it $t(f)$, with its module $|t(f)|$ and its phase $\angle t(f)$, from which it is possible to find the transmittance, the group delay, and the dispersion defined by

$$T(f)[\mathrm{dB}] = 20\log_{10}|t(f)| \tag{9}$$

$$\tau_d(f) = -\frac{1}{2\pi}\frac{\partial \angle t(f)}{\partial f} \tag{10}$$

$$\mathrm{CD}(\lambda) = \frac{\partial \tau_d(\lambda)}{\partial \lambda}. \tag{11}$$

The inputs to the model are the same as those in the last test, plus the following with respect to the AW grating order and the OW mode field:

1) IW taper W_i and spatial modal field $b_i(x_0)$, where x_0 is the IW coordinate;
2) OW taper W_o and spatial modal field $b_o(x_3)$, where x_3 is the OW coordinate;
3) slab couplers length L_f;
4) slab refractive index $n_s = 1.430\,26$;
5) AW spacing d_w;
6) AW number $N = 499$;
7) Design frequency $f_0 = 193.95$ THz;
8) grating order m;
9) AW length increment ΔL.

In addition, the AWG channel to be verified is number 24 in the AOUK design, with a target frequency of 194.1 THz. These design parameters correspond to a 1 × 40 AWG with 100-GHz channel spacing. Besides these inputs, further assumptions have to be made regarding the AW amplitude and phase distributions to be used in the simulation, since both phase distributions measured by FS and the simulated in the previous section are available. The use of the simulated field distribution would yield the ideal transfer function for the AWG, since as can be seen in Fig. 3, the ideal AW field distribution does not contain any fabrication imperfection. To take into account the fabrication errors, the measured AW field distribution can be used instead, or even only part of it—the amplitude, the phase, or both. This is one of the advantages of having a piecewise modeling, and it is also an approach that has been used by other authors that investigate the impact of the imperfections with a formulation similar to (1), as for instance in [21]. We tried all the possible combinations—amplitude errors only, phase errors only, and amplitude and phase errors together. The best match with the measured transmittance was obtained when using only the measured phase distribution, along with the simulated amplitude for the AW field distribution $B_i(x_1)$. This is consistent with the conclusions of Section II-A in which the simulated amplitude revealed some details that are not captured by the FS method. Moreover, as the measured phase distribution is used, no extra defocusing in the slabs is included, since it is already contained in it. Notice also that not all of the measured phase distribution can be used in the simulations, since some parts are noisy, as can be observed in Fig. 3. As commented at the end of Section II, only the measured data obtained from the central waveguides in the array is usable.

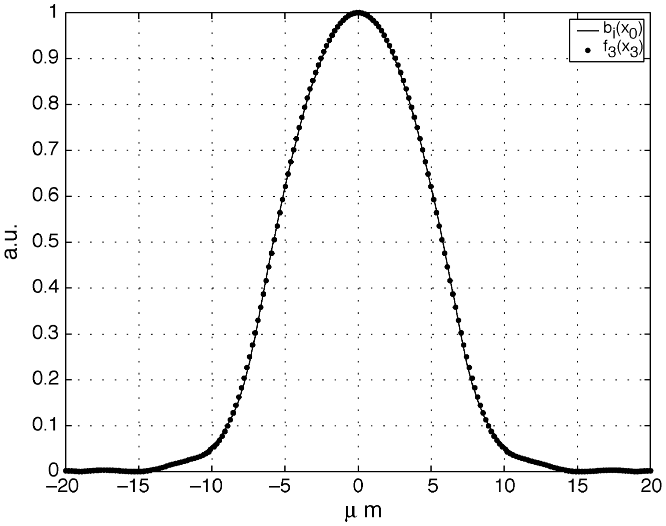

Fig. 4. IW mode field $b_i(x_0)$ (solid line) and lens pattern $f_3(x_3)$ (dots).

A. Transmittance

The results for the inputs and assumptions described previously are shown in Fig. 5(a) and (b). The first plot is an enlarged view of the second one, to show the simulated bandwidth shape versus the measured one, which at a glance are in good agreement. To be more precise, the bandwidths at 1 and 3 dB have also been compared. For the measurement, the bandwidths are $bw_{1\mathrm{dB},m} = 32.672$ GHz and $bw_{3\mathrm{dB},m} = 55.290$ GHz, respectively, while for the simulation, they are $bw_{1\mathrm{dB},s} = 33.250$ GHz and $bw_{3\mathrm{dB},s} = 55.850$ GHz. The differences are 0.578 and 0.560 GHz for 1- and 3-dB points bandwidths. The match is good since the difference is of approximately 2% and 1%, respectively. The second plot in the same figure shows the floor level of the transmittance, i.e., the level of the AWG response out of the passing band. It is well known that this level is due to fast phase errors [22], i.e., the rapid variations over the measured

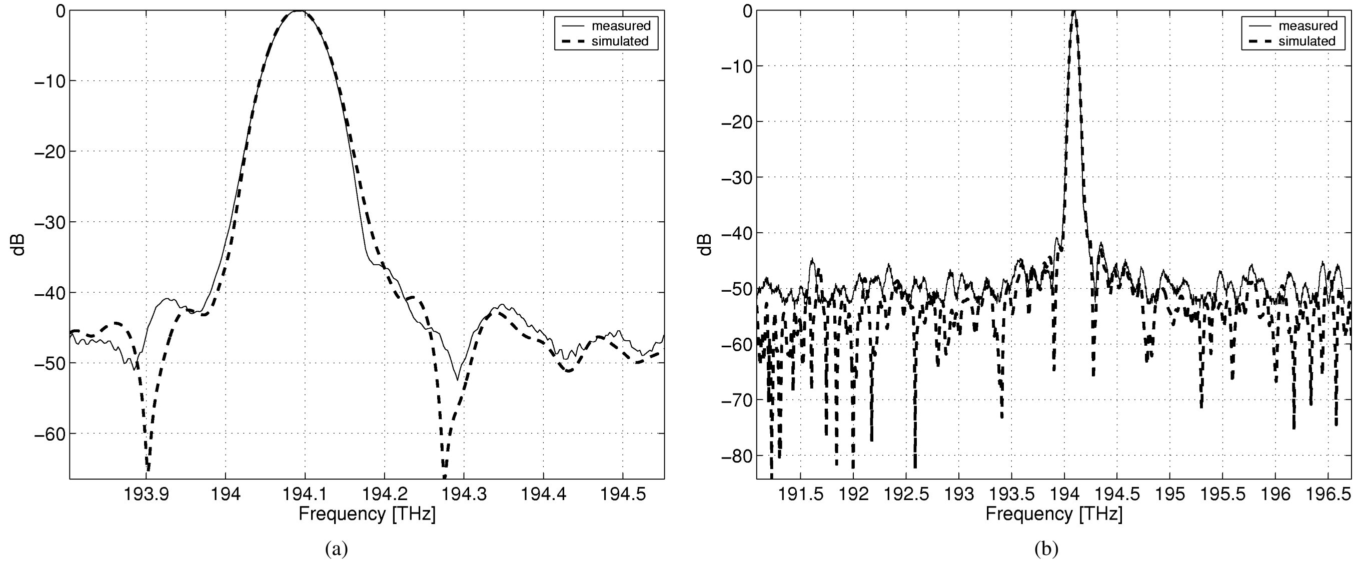

(a) (b)

Fig. 5. Transmittance (normalized to the maximum) (in decibels) measured (solid line) and simulated (dashed line). (a) Passband detail. (b) Floor-level detail.

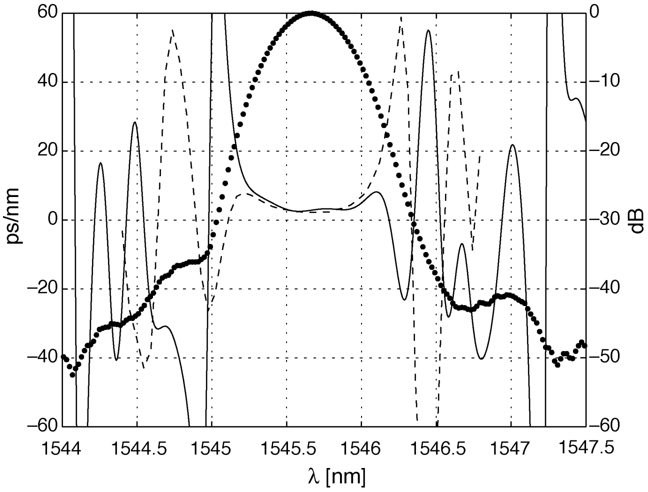

Fig. 6. Left axis (picoseconds per nanometer): Dispersion measured (solid line) and simulated (dashed line). Right axis (decibels): Normalized simulated transmittance (dotted line).

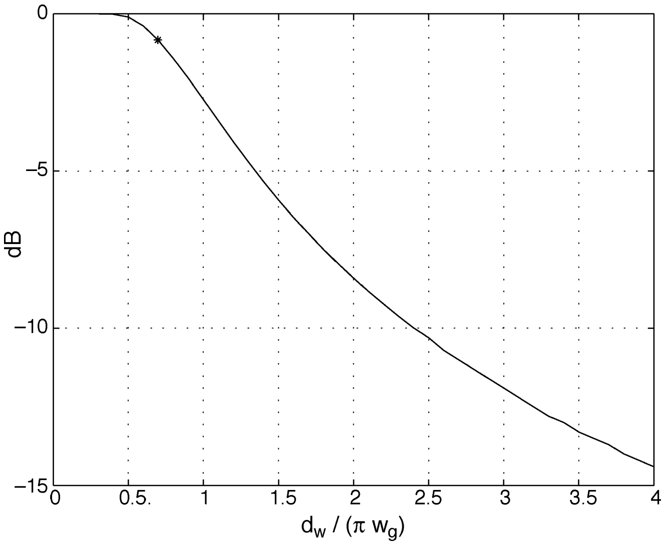

Fig. 7. Diffraction loss (solid line) and the particular value for the AWG design under analysis (asterisk) estimated with the model.

curved phase distribution in Fig. 3(b). The use of the measured AW phase distribution in the simulations yields a floor level matching the one in the measurement. Therefore, under the previously mentioned assumptions, the transmittance passing band shape, bandwidth, and floor level are well reproduced by the model.

B. In-Band Dispersion

One of the possibilities of the model is to retrieve numerically the phase information [13] for the transfer function $\angle t(f)$, and thus the in-band dispersion of the filter using (11), which is not possible following the approaches that use (1). The simulation results are compared with the dispersion measurements in Fig. 6, where the transmittance has also been plotted to distinguish clearly the in-band dispersion. The dispersion is mainly due to the slow errors on the AW phase, as concluded in [22], i.e., the slight phase curvature present in Fig. 3(b). The shape of the dispersion curves is very similar inside the 20-dB bandwidth points of the transmittance. Outside the band, the dispersion differs. Notice that for this parameter, it is more difficult to match exactly the measured magnitude, although the simulated values are in the order of the measured. This may be due to the FS measurement precision of the phase errors, as mentioned in [15]. Despite this, the match is good for the in-band dispersion values, which are the relevant ones.

C. Insertion Loss

The measured insertion loss for channel 24 at 194.1 THz is 2.76 dB. There are several loss factors in the AWG, as described for instance in [10] and [13].

1) Diffraction Loss: The diffraction loss corresponds to the two transitions SC 1 to AWs and AWs to SC 2, and it is related to the AW mode- field radius w_g and the AW spacing d_w [10]. Fig. 7 shows the diffraction loss for different values

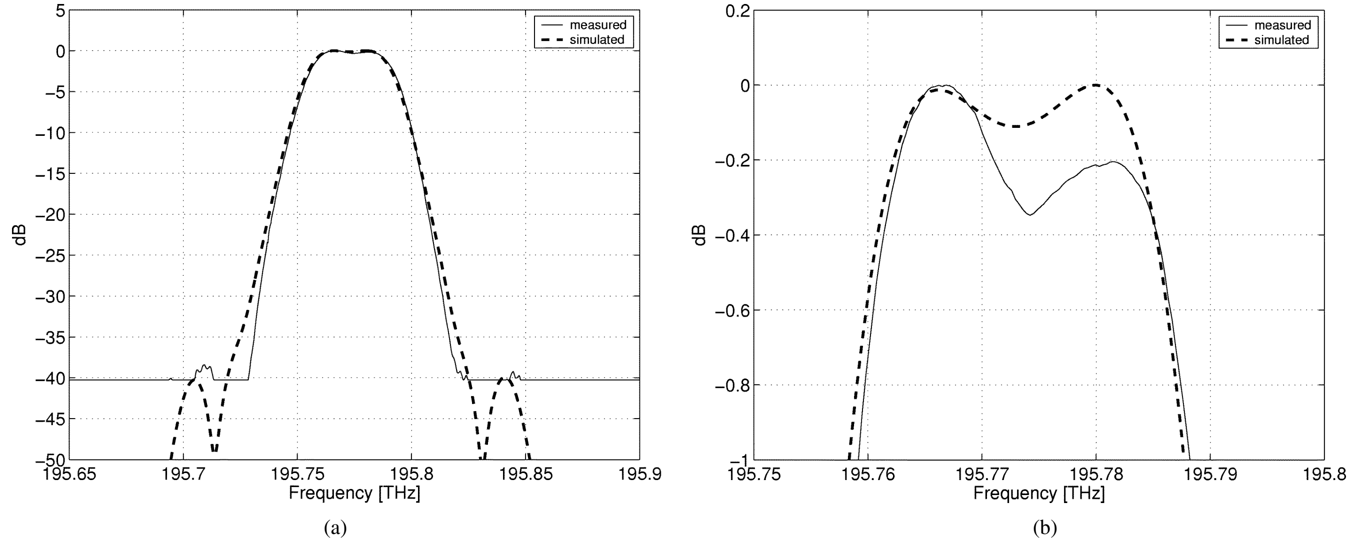

Fig. 8. Transmittance (in decibels) measured (solid line) and simulated without fabrication errors (dashed line). (a) Full-band view. (b) Top view.

of $d_w/(\pi w_g)$ and the estimated for the AWG design provided by AOUK following the method in [13]. The estimation from AOUK is 0.4 dB for each AW–SC transition, i.e., 0.8 dB for both. The estimation using the model is 0.8268 dB for the total, close to the expected.

2) Coupling to Output Waveguide: The coupling loss is related to the overlap of the lens pattern $f_3(x_3)$ and the OW mode field $b_o(x_3)$. It can be calculated numerically with the overlap integral of the lens pattern with the OW mode field for perfect alignment (that is, for a frequency $f = 194.1$ THz corresponding to the center of the passing band of the output port number 24 being considered in this analysis). The result is 0.0269 dB of loss. Under ideal conditions, it should be 0 dB, since the lens pattern should be a perfect image of the IW mode field, equal to the OW. The difference arises from a small truncation and the phase errors, both in the AWs.

3) Fiber Butt-Coupling, Propagation, and Calibration Loss: These losses have been estimated and provided by AOUK and are not simulated in the model, which only reproduces the IW–OW losses. The nonoptimized fiber butt-coupling loss is 0.5 dB for each fiber attached to the waveguides, which makes a total of 1 dB, due to the input and output fibers. The propagation loss, due to the maximum length of the device, with an insertion loss coefficient of 0.025 dB/cm, is 0.7 dB. Finally, the error estimated for the measurement method is 0.2 dB.

4) Total Loss: With the two predictions from the model, diffraction and coupling to the OW loss, and the inputs provided by AOUK, the total loss is 2.8268 dB, very close to the measurement 2.76 dB. Therefore, the part of the insertion loss due to internal changes in the design of the AWG is well reproduced by the model.

D. Conclusions for the AWG-G Modeling

In this section, the model has been validated for Gaussian AWG devices. The measured transmittance shape, bandwidth, and floor level, the in-band dispersion, and the insertion loss are reproduced by the model. The design data provided by AOUK and the FS measured phase errors were used in the model. Therefore, the model is suitable not only to design AWG devices, but also to investigate in a piecewise manner, which is the impact of the different sources of errors in the AWG response.

V. FULL FLAT-TOP AWG MODEL VALIDATION

The choice of the Gaussian AWG type to start the model validation follows after the natural evolution that has taken place in the AWG market: a shift from Gaussian (a relatively simple device) to flat-top (more complex structure) devices. Once the model has been validated for AWG-G devices, the study of AWG-F devices follows. The AWG-F design and measurements given by AOUK for the analysis correspond to a 1 × 8 AWG with 50-GHz channel spacing. The AWG-F flat-top operation is attained by a multimode structure placed at the input side of the first SC. It provides a double-peaked mode field at its output. This field is imaged to the output side of the second SC, yielding a flat-top transmittance when overlapped with the OW mode. The following design data are supplied by AOUK:

1) IW multimode structure size W_i and spatial modal field $b_i(x_0)$, where x_0 is the IW coordinate;
2) OW width W_o and spatial modal field $b_o(x_3)$, where x_3 is the OW coordinate;
3) slab couplers length L_f;
4) slab refractive index $n_s = 1.430\,26$;
5) AW spacing d_w;
6) AW number $N = 469$;
7) design frequency $f_0 = 195.725$ THz;
8) grating order m;
9) AW length increment ΔL.

To establish a reference case for the analysis, a simulation with this design data and without fabrication errors is performed. The results are shown in Fig. 8, compared with the measured spectra. The measurement is performed only to −40 dB from the maximum, since the interest is concentrated in the passband. The floor level may not be relevant, because it is a 1 × 8 device [23]. In order to yield a good performance, the AWG-F should have a passband resembling a box-like function, symmetric and

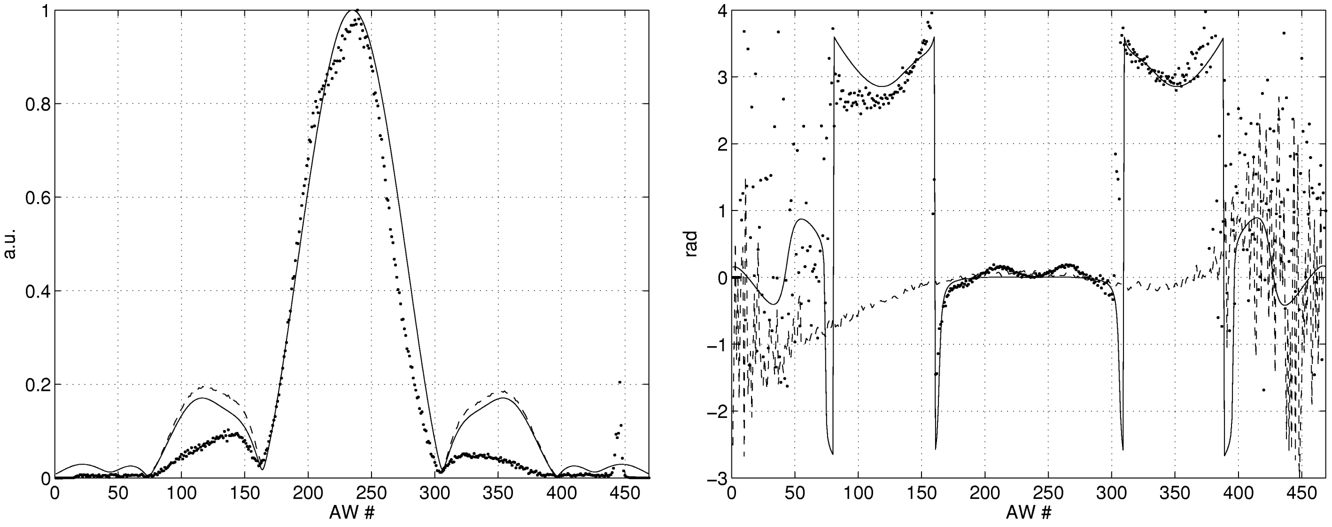

(a) Amplitude

(b) Phase

Fig. 9. AW field distribution FS measurements for the AWG-F under study: (a) amplitude ideal (solid line), measured (dotted line), and forced asymmetry (dashed line) and (b) phase ideal (solid line), measured (dots), and measured without horn at the input side (dashed line).

with a very flat top. The simulation results are shown in dashed lines in the figure, where the passband and an enlarged view of its top are shown. For this design case, the passband roll-off of the fabricated device is very close to the ideal one, as shown in Fig. 8(a), down to -20 dB. However, there are significant differences on the top of the passing band, plotted in Fig. 8(a). Referring to this figure, and to quantify the differences, two parameters are used: the passband ripple, defined as the difference between the passband maximum and the passband dip, and the passband asymmetry, which is the difference between the two passband peaks. While the ideal design is very symmetric, and the passband ripple is low (about 0.1 dB), the fabricated device exhibits an asymmetry of 0.2 dB and a ripple of 0.35 dB, as shown in Fig. 8(a).

Therefore, these degradations are due to fabrication errors, and they are going to be investigated in this section. As for the AWG-G, FS measurements of the device have been performed. They are shown in Fig. 9, along with the ideal AW field distribution from the simulation without fabrication errors versus the AW number (the waveguide length increases with the AW number).

Concerning the AW amplitude distribution, in Fig. 9(a), several discrepancies are found comparing it with the ideal one. First, the size of the sidelobes is lower in the measurement than in the ideal simulation. Second, the measured amplitude distribution is asymmetric, i.e., the sidelobes do not have the same level. We believe that the most likely cause for the former is the sidelobe cancellation, as concluded in Section II-A, while the cause for the latter could be errors in n_{eff} in the long waveguides, as explained in [24].

Regarding the phase distribution for the AWs, in Fig. 9(b), there are several discrepancies also between the ideal (solid line) and the measured (dots). First, for the center AWs, there is a phase ripple in the measurement, while the ideal distribution indicates this part should be flat. Second, for the AWs where the amplitude sidelobes are, there is an additional curvature, down for waveguides between 75 to 125 and up for waveguides 350 to 390 approximately. As mentioned previously, with the FS setup in Fig. 2, an end-to-end measurement is performed. Therefore, present in the result are not only the errors due to the SCs and the AWs, but also in this case any kind of phase and amplitude error due to the input horn. In order to distinguish the different contributions to the phase errors, we performed a measurement of another identical device with the same design, but replacing the input horn with a regular IW of width 6 μm. The phase error for the latter case is shown with a dashed line in the same figure [Fig. 9(b)], and it exhibits the down and up trend observed and commented on previously for the same waveguides. Moreover, no ripple is present for the center waveguides, and therefore we can conclude that the ripple is due to the input horn, while the slow phase curvature is due to the SCs and the AWs.

Hence, the investigation along these subsections will focus on how all of these errors affect the bandwidth at 0.5, 1, 3, and 20 dB points, the passband dip (or ripple), and the passband asymmetry. The analysis will be carried out with different combinations of the measured and simulated results for the AWs in order to identify which errors are responsible for which degradations in the response, in a similar way as we did for the AWG-G in Section IV.

A. Simulation With the Measured AW Amplitude and Phase Errors

In this case, we perform the simulation neglecting the AW's field distribution produced by the Fresnel diffraction integral in the first SC. Instead, we substitute it by the measured one, represented in dots in Fig. 9(a) and (b), and perform the simulation for the rest of the device, the phase change of the AWs, the Fresnel integral for the second SC, and the overlap integral for the OW [13]. The transmittance obtained is shown in Fig. 10 in dashed lines. The discrepancies with the measured transmittance are present outside and inside the passband. The result leads to the same conclusion as that for the AWG-G: the FS measurements cannot be directly utilized as the field distribution for the AW in our simulation model. Therefore, the FS measurements must be

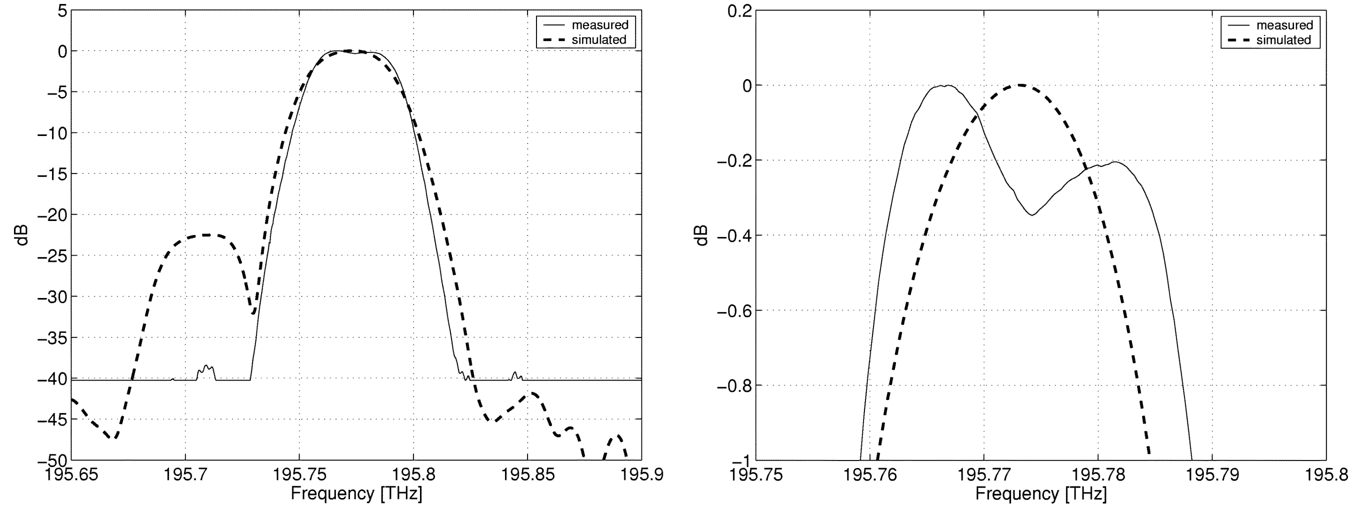

(a) (b)

Fig. 10. Transmittance (in decibels) measured (solid line) and simulated with the measured AW amplitude and phase (dashed line). (a) Full-band view. (b) Top view.

processed and combined with the ideal AW field distribution in a similar way as for the AWG-G.

B. Simulation With Only the AW-SC Phase Errors

Hence, in this case, we investigate the impact of the phase errors due to the slabs and the AWs, which were measured and shown in Fig. 9(b) with a dashed line. To include these errors in the numerical simulations, first the Fresnel integral is solved numerically for the first SC, and the ideal amplitude and phase distributions for the AWs are obtained, as shown in Fig. 9(a) and (b) with solid lines. Second, the ideal phase is modified accordingly to the AW–SC phase errors, i.e., the latter is added to the former, while the ideal AW amplitude is kept. After this numerical manipulation, the rest of the device is simulated, as indicated in the previous section. The result obtained for the transmittance is shown in Fig. 11. First, the enlarged view (a) shows a good match in the roll-off of the filter down to −40 dB, and moreover, the measurement floor level is not exceeded as in the previous case. Second, there is an asymmetry in the simulated transmittance passband top, shown in Fig. 11(b). Note that the asymmetry is in the same direction as that in the measurement (the contrary would mean that an error exists in the simulator) and that the value is 0.16 dB, which, compared with the measurement 0.2 dB, is a fairly good approach. However, the result is no so good for the passband ripple, which for the simulation is approximately 0.13 dB, while for the measurement, it is 0.35 dB, as indicated previously.

The results seem to demonstrate that the asymmetry in the passband top is mainly due to the AW–SC phase errors. To confirm this fact, we performed another simulation with a similar device design whose transmittance measurements showed high passband asymmetry and little ripple. We proceed in a similar way as that described in the previous paragraph, with the AW phase errors. The result is shown in Fig. 11(c) and (d). The transmittance obtained through simulation has a passband asymmetry of approximately 0.77 dB, while the measurement has 0.92 dB. Again, the difference between the simulation and the measurement is very low, and then it is possible to conclude that in the AWG-F designs under test, the main source of passband asymmetry is the AW–SC phase errors.

C. Numerical Fit Using AW Field Modified With the Aid of FS Results

The conclusions from the previous section lead to the investigation of the passband ripple, since it has not been properly reproduced by the simulations when using only the AW–SC phase errors. In the following simulation, we included the AW–SC phase errors as well, as in the previous subsection. Besides this, we also modified the ideal AW field amplitude distribution to push some asymmetry on the sidelobes, in a similar way to the measured AW amplitude distribution represented with dots in Fig. 9(a). This is shown in the same figure with a dashed line. After this, we performed the simulation of the rest of the device as before and obtained the transmittance shown in Fig. 12. The subplot (b) shows how the ripple is increased with respect to Fig. 11(b) when some asymmetry is included in the AW's amplitude distribution. The measurement shows a ripple of 0.35 dB, and the simulation has 0.25 dB. However, note also that the passband asymmetry is reduced to 0.1 dB, which, compared with the former case, is a reduction of 0.06 dB. Hence, the joint conclusions from these two subsections are the following: the passband ripple and asymmetry are related to both the AW amplitude asymmetry and the AW–SC errors. Nevertheless, the passband asymmetry is mainly governed by the AW–SC errors, while the ripple is mainly due to the AW amplitude asymmetry.

There is still a magnitude that has not been cited: the bandwidth. The 0.5-, 1-, 3-, and 20-dB bandwidths (the n-dB bandwidth is the difference, in wavelength or frequency, between the points at which the transmittance falls n dB at both sides of its maximum) for the cases under study are shown in Fig. 13(a). The percent bandwidth error (PBE) with respect to the measurement, labeled as AOUK in the figures, is also shown in

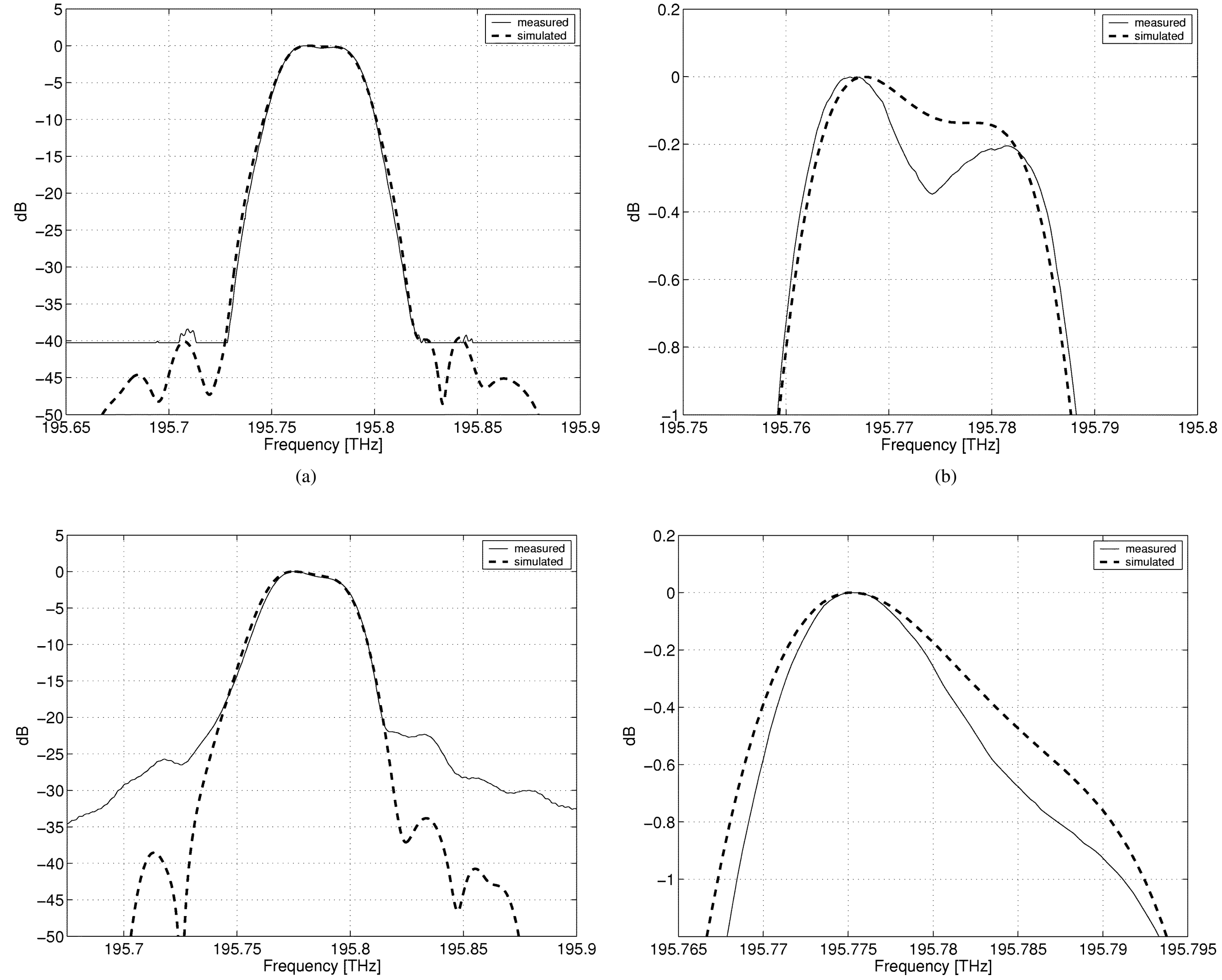

(a) (b)

(c) (d)

Fig. 11. Transmittance (in decibels) measured (solid line) and simulated with only AW–SC phase errors (dashed line). (a) First AWG-F, full-band view. (b) First AWG-F, top view. (c) Second AWG-F, full-band view. (d) Second AWG-F, top view.

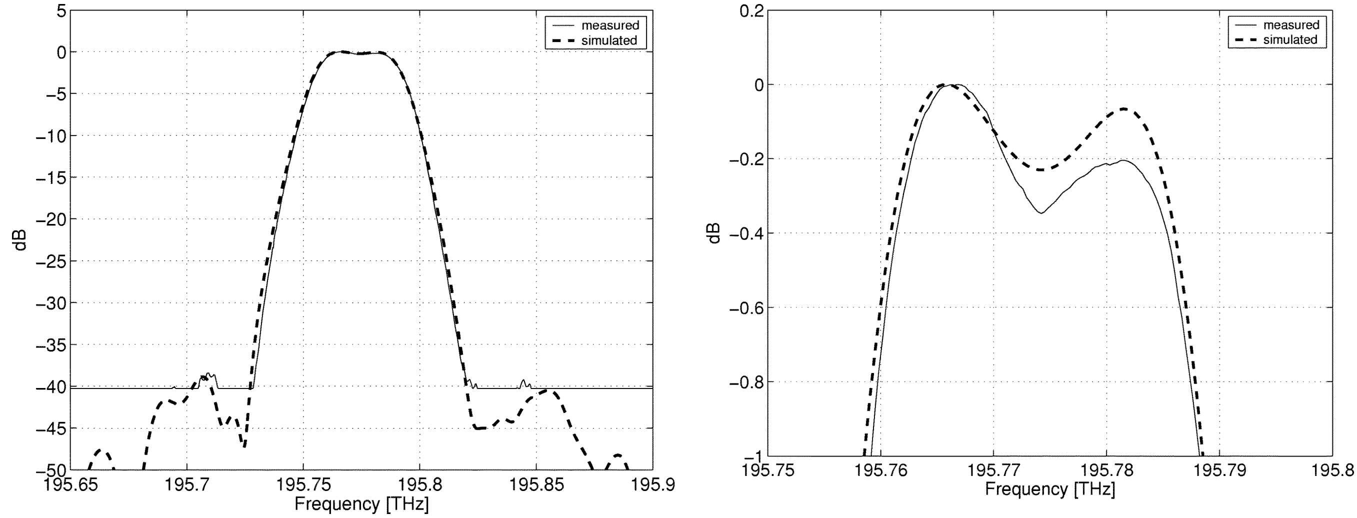

(a) (b)

Fig. 12. Transmittance (in decibels) measured (solid line) and simulated with AW–SC phase errors and amplitude synthesized amplitude asymmetry (dashed line). (a) Full-band view. (b) Top view.

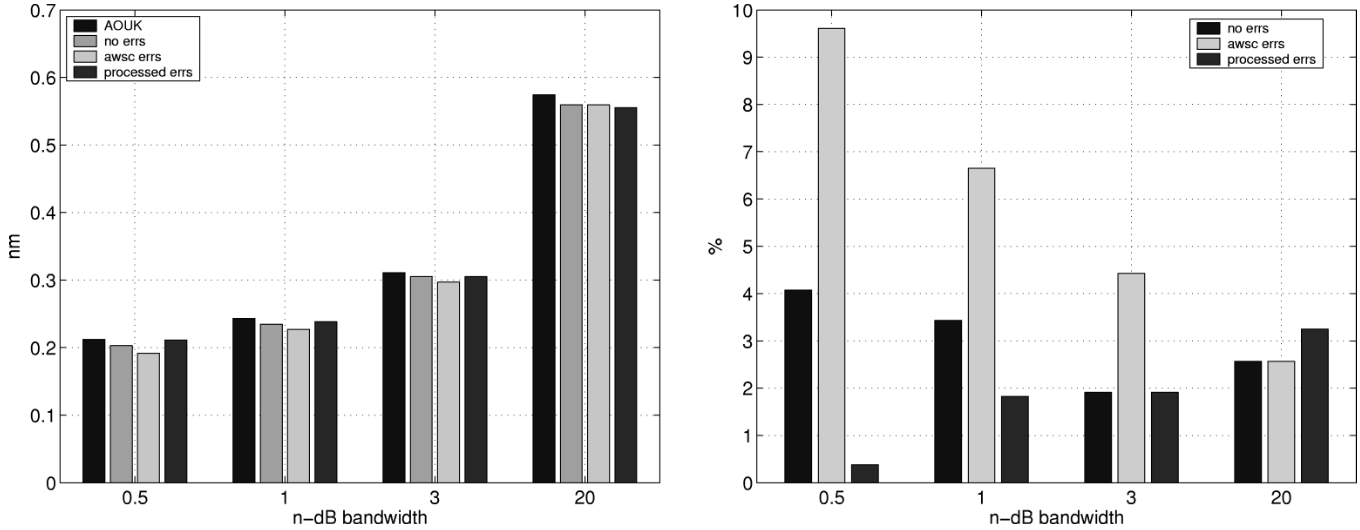

(a) Bandwidth

(b) Percent Error

Fig. 13. (a) Bandwidth analysis and (b) percent error for the AWG-F transmittance tests.

Fig. 13(b). As can be seen, the best match regarding the bandwidth points corresponds to the last simulation case, in which the AW–SC phase errors and the AW amplitude asymmetry are taken into account, with deviations from the measured bandwidth below the 2% for 0.5-, 1-, and 3-dB bandwidths and less than 4% for the 20-dB bandwidth. The following additional conclusions can be derived observing the PBE from Fig. 13(b). First, when the AW ideal amplitude and phase are used, the PBE is less than 4% for all the points. In this case, the simulated passband was very symmetric (Fig. 8), and therefore the highest error is on the top of the passband, at the 0.5-dB bandwidth point. Second, when using only the AW–SC errors, although the asymmetry is better approximated (Fig. 11), the PBE is bigger for the 0.5-, 1-, and 3-dB bandwidth. Therefore, the asymmetry approximation using only AW–SC increases the PBE on the top of the band. Finally, when using the AW–SC phase errors with some AW amplitude asymmetry (labeled as "processed" in the figure), the top of the band trend was better reproduced [Fig. 12(b)], which is consistent with the PBE shown in Fig. 13(b), the lowest of all the cases presented previously. Notice also that comparing the case without errors (ideal situation) and with processed errors (closest to the real device), the latter have direct impact on the top of the band. For instance, the PBE at 0.5 dB is very low for the latter. Moreover, in none of the cases is the impact significant on the lowest part of the passing band (20-dB point). This is consistent with the conclusions from [22], where the floor level and close points from the passing bands were shown to be affected by fast rather than slowly varying errors, which are the ones included with the AW–SC phase errors.

Note that we have reached these partial conclusions without taking into account the errors due to the input horn that have been skipped in all the simulations by retaining only the AW–SC phase errors. Moreover, errors in the input horn can also lead to asymmetries in the amplitude of the field distribution for the AWs. Therefore, we could conclude that the rest of ripple and asymmetry is due to the horn errors. To confirm this, we provide an additional simulation case to exemplify how an improper design of the multimode structure at the input side of the device can lead to these kinds of errors. The situation proposed consists on an off-center-fed multimode interference (MMI) coupler [25]. The MMI is also used to produce a double-peaked image for flat-top AWG devices, similar to the one provided by a waveguide horn. The MMI design is the following: width 17 μm and length 198 μm, and it is fed by a 6μm waveguide offset by -0.15 μm from the MMI center. The input, propagation, and output field intensities are shown in Fig. 14. The intensity for the output mode is shown in Fig. 15(a), along with the horn mode provided by AOUK for the previous tests, which was found using a mode solver, and it is not measured from the AWG under test. The off-center feeding of the MMI yields an asymmetric double-peaked output mode, as represented in Fig. 15(a) with a dashed line. The amplitude of the diffraction of the asymmetric MMI mode through SC 1 is shown in Fig. 15(b), and it exhibits asymmetric sidelobes as the FS measurement in Fig. 9(a) for the AWG-F device.

The AWG design parameters for this simulation case are the same as previously, and only the input horn mode is replaced by the previously mentioned asymmetric MMI mode. The obtained transmittance is shown in Fig. 15(c) and (d). In (c), the passband shape is shown for the simulation and the measurement. The differences that arise at the lower part of the passing band are due to the differences between the MMI and horn modes, rather than the asymmetry. This is mainly due to the different fall from the maximum in the modes, as can be checked in Fig. 15(a) from -15 to -5 μm. A close look at the passband top [Fig. 15(d)] shows how the AW amplitude asymmetry accentuates the passband deep, while the asymmetry between the passband peaks is also leveraged. The same AW–SC phase errors than before have been added to the simulated AW phase distribution, which has been obtained from the diffraction through SC 1 of the MMI mode.

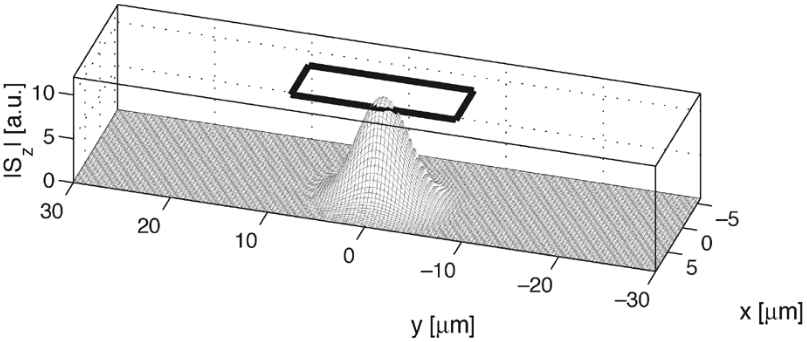

(a) Input 6 micron mode

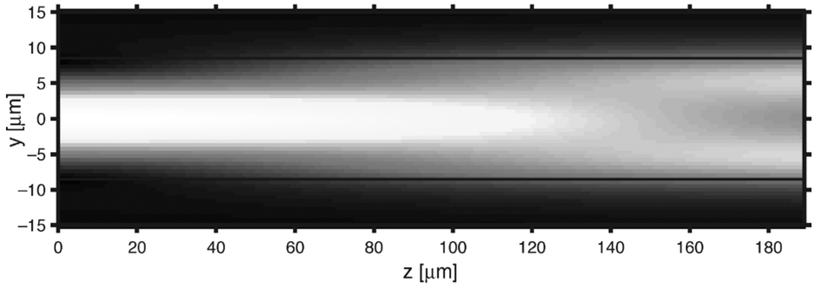

(b) MMI propagation

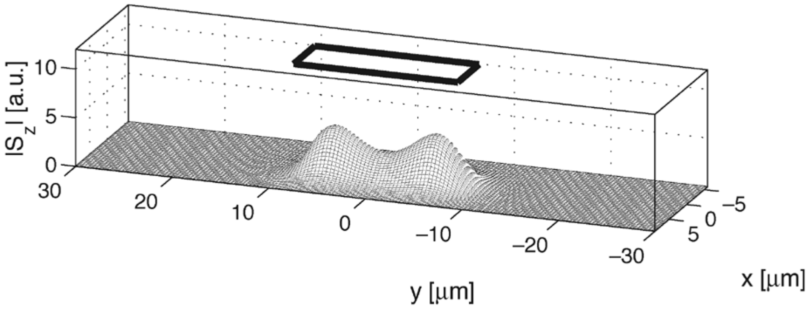

(c) Output mode

Fig. 14. MMI (a) input, (b) propagation, and (c) output modal intensities.

Hence, the joint conclusion of these sections is that the asymmetry and deep in the passband are due to both the AW–SC errors and the asymmetry in the AW amplitude distribution.

VI. CONCLUSION

This pape has presented the validation of the AWG Fourier optics-based mathematical model presented in [13] using the design data, measured spectrums, and amplitude and phase errors of previously fabricated AWGs. First, the validity of the SC modeling was explored. The modeling of the SCs is performed numerically with the evaluation of the Fresnel diffraction integral, rather than the Fourier transform, to yield exact results. The measured AW field distribution, amplitude, and phase were compared for Gaussian and flat-top devices with the simulated diffraction, and some discrepancies were revealed that, after an analytical cross-check of the numerical simulations and conclusions from other authors in the literature, it is believed are due to the FS measurement method. Thus, it is concluded that the FS measurements cannot be used directly in this modeling tool, but rather they must be combined with results from the simulations and processed properly.

The validation of the full model, SCs, phase change in the AWs, and overlap integral for the OWs was carried out first for Gaussian AWG devices, for which, in a particular design case, the transmittance obtained with the model matched the passband shape, bandwidth, and floor level of the measured transmittance. Moreover, the in-band dispersion, also given by the model, and the insertion loss, are in good agreement with the measured one.

After the model validation for Gaussian AWG devices, the formulation and numerical tool was used to establish relationships between the fabrication errors and the degradations present in flat-top AWG devices. Two different fabricated devices were studied under different simulation cases, each corresponding to different assumptions on the fabrication errors. It was concluded that the passband asymmetry in AWG-F devices is mainly due to AW–SC phase errors and that the passband ripple is mainly determined by the asymmetry of the amplitude of the field distribution in the AWs. However, it was observed that a small part of the ripple and passband asymmetry is also determined by the combination of both the AW–SC phase errors and the AW amplitude asymmetry. This was determined with an additional simulation case, in which the possibility of an incorrect design was considered in the input multimode structure used to make the AWG flat-top.

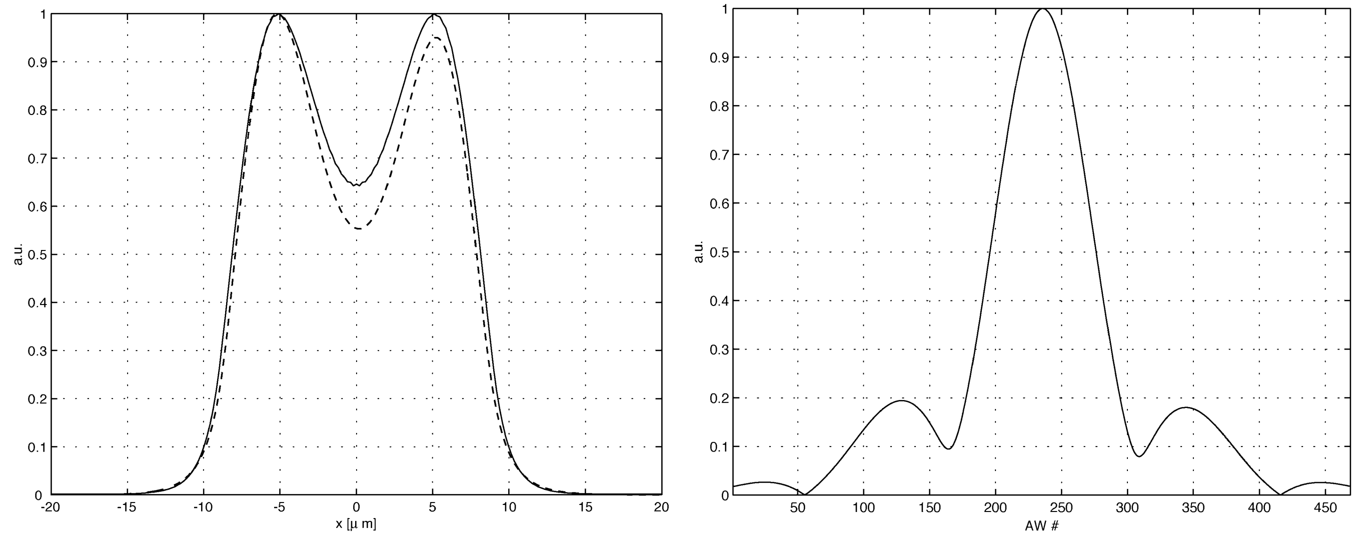

(a) Horn and MMI modes (b) AW amplitude for the MMI

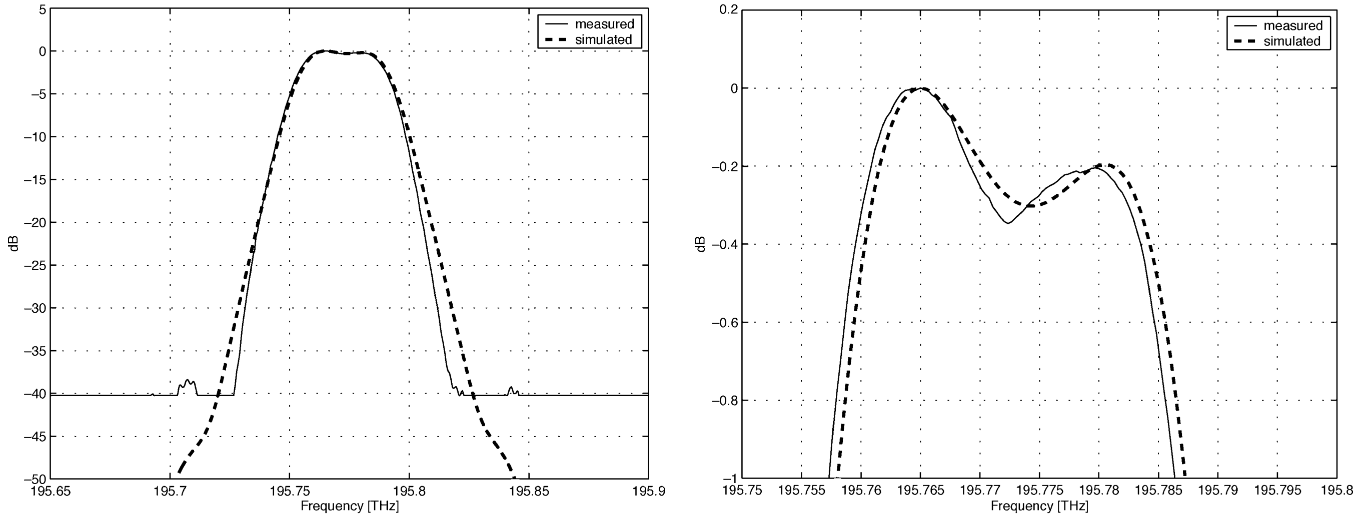

(c) Full band view (d) Top view

Fig. 15. (a) Horn (solid line) and off-center-fed MMI mode fields (dashed line). (b) AW field distribution for the MMI field. (c) Transmittance measured (solid line) and simulated with the off-center-fed MMI AW field distribution (dashed line). (d) Zoomed view.

Hence, it has been proven how a piecewise modeling, such as that used throughout this paper, is more useful and flexible in deriving precise conclusions about the impact of each kind of fabrication error, which cannot be analyzed using other models, as for instance, the ones using formulations similar to (1).

The performance analysis with this piecewise model can be very helpful for AWG manufacturers, since the causes of response degradations after fabrication can be identified and isolated, to some extent, as has been shown in this paper. Therefore, feedback data can be provided to the designers, which can be used to apply corrections to their designs at precise parts of the device, for example, the slabs, the array, or other construction elements in an AWG.

ACKNOWLEDGMENT

The Avanex team would like to thank D. McMillan for performing Fourier transform spectroscopy measurements.

REFERENCES

[1] M. Smit, "New focusing and dispersive planar component based on an optical phased array," *Electron. Lett.*, vol. 24, pp. 385–386, Mar. 1988.

[2] H. Takenouchi, H. Tsuda, and T. Kurokawa, "Analysis of optical-signal processing using an arrayed-waveguide grating," *Optics Express*, vol. 6, pp. 124–135, Mar. 2000.

[3] Y. Yoshikuni, "Semiconductor arrayed waveguide gratings for photonic integrated devices," *IEEE J. Select. Topics Quantum Electron.*, vol. 8, pp. 1102–1114, Nov./Dec. 2002.

[4] H. Takahashi, S. Suzuki, and I. Nishi, "Wavelength multiplexer based on $SiO_2 - Ta_2O_5$ arrayed waveguide grating," *J. Lightwave Technol.*, vol. 12, pp. 989–995, June 1994.

[5] ——, "Multiwavelength ring laser composed of edfas and an arrayed-waveguide wavelength multiplexer," *Electron. Lett.*, vol. 30, pp. 44–45, Jan. 1994.

[6] D. Huang, T. Chin, and Y. Lai, "Arrayed waveguide grating DWDM interleaver," in *Proc. Optical Fiber Communications Conf.*, vol. 3, 2001, pp. WDD80 1–WDD80 3.

[7] H. Takahashi, K. Oda, H. Toba, and Y. Inoue, "Transmission characteristics of arrayed waveguide N × N wavelength multiplexer," *J. Lightwave Technol.*, vol. 13, pp. 447–455, Mar. 1995.

[8] C. Dragone, "An $N \times N$ optical multiplexer using a planar arrangement of two star couplers," *IEEE Photon. Technol. Lett.*, vol. 3, pp. 812–815, Sept. 1991.

[9] C. Dragone, C. Edwards, and R. Kistler, "Integrated optics $N \times N$ multiplexer on silicon," *IEEE Photon. Technol. Lett.*, vol. 3, pp. 896–898, Oct. 1991.

[10] M. K. Smit and C. van Dam, "PHASAR-based WDM-devices: Principles, design and applications," *IEEE J. Select. Topics Quantum Electron.*, vol. 2, pp. 236–250, June 1996.

[11] R. Marz, *Integrated Optics, Design and Modeling*. Norwood, MA: Artech House, 1994, ch. 8, pp. 251–281.

[12] M. C. Parker and S. D. Walker, "Design of arrayed-waveguide gratings using hybrid Fourier–Fresnel transform techniques," *IEEE J. Select. Topics Quantum Electron.*, vol. 5, pp. 1379–1384, Sept./Oct. 1999.

[13] P. Muñoz, D. Pastor, and J. Capmany, "Modeling and design of arrayed waveguide gratings," *J. Lightwave Technol.*, vol. 20, pp. 661–674, Apr. 2002.

[14] J. W. Goodman, *Introduction to Fourier Optics*, 2nd ed. New York: McGraw-Hill, 1994, ch. 4 and 5.

[15] K. Takada, H. Yamada, and Y. Inoue, "Optical low coherence method for characterizing silica-based arrayed-waveguide grating multiplexers," *J. Lightwave Technol.*, vol. 14, pp. 1677–1689, July 1996.

[16] C. D. Lee, W. Chen, Q. Wang, Y.-J. Chen, W. T. Beard, D. Stone, R. F. Smith, R. Mincher, and I. R. Stewart, "The role of photomask resolution on the arrayed waveguide grating response," *J. Lightwave Technol.*, vol. 19, pp. 1726–1733, Nov. 2001.

[17] K. Okamoto, *Fundamentals of Optical Waveguides*. London, U.K.: Academic, 2000, ch. 2, pp. 13–45.

[18] W. Chen, Y.-J. Chen, M. Yan, B. McGinnis, and Z. Wu, "Improved techniques for the measurement of phase error in waveguide based optical devices," *J. Lightwave Technol.*, vol. 21, pp. 198–205, Jan. 2003.

[19] R. N. Bracewell, *The Fourier Transform and Its Applications*, ser. Electrical Engineering. New York: McGraw-Hill, 1986.

[20] S. S. Soliman and M. D. Srinath, *Continuous and Discrete Signals and Systems*, 2nd ed. Englewood Cliffs, NJ: Prentice-Hall, Dec. 1997.

[21] K. Takada, Y. Inoue, H. Yamada, and M. Horiguchi, "Measurement of phase error distributions in silica-based arrayed-waveguide grating multiplexers by using fourier transform spectroscopy," *Electron. Lett.*, vol. 30, pp. 1671–1672, Sept. 1994.

[22] P. Muñoz, D. Pastor, J. Capmany, and S. Sales, "Analytical and numerical analysis of phase and amplitude errors in the performance of arrayed waveguide gratings," *IEEE J. Select. Topics Quantum Electron.*, vol. 8, pp. 1130–1141, Nov./Dec. 2002.

[23] P. Muñoz, D. Pastor, and J. Capmany, "Cross talk floor statistical analysis of arrayed waveguide gratings," presented at the IEEE/LEOS Workshop Fiber Optics Passive Components, Glasgow, U.K., June 2002.

[24] T. Gob, S. Suzuki, and A. Sugita, "Estimation of waveguide phase error in silica-based waveguides," *J. Lightwave Technol.*, vol. 15, pp. 2107–2113, Nov. 1997.

[25] P. Muñoz, D. Pastor, and J. Capmany, "Analysis and design of arrayed waveguide gratings with MMI couplers," *Optics Express*, vol. 9, pp. 328–338, Sept. 2001.

Pascual Muñoz (S'03) was born in Albal, Spain, on February 7, 1975. He received the M.Sc. Ingeniero de Telecomunicación degree from the Universidad Politécnica de Valencia (UPV), Valencia, Spain, in 1998. He is currently working toward the Ph.D. degree with the Optical Communications Group at UPV.

He previously worked as an IT Consultant for AIMME Instituto Tecnológico on Paterna, Valencia, Spain, while collaborating with the Optical Communications Group (OCG) of UPV in Optical Network Planning software development for Telefonica I+D in 1999. In July 1999, he joined the Spanish Air Force as Second Lieutenant. Since January 1, 2000, he has been an Researcher/Lecturer at UPV. His main interests are in arrayed-waveguide grating (AWG) devices for implementing optical layer network functions and optical network planning simulation software development.

Mr. Muñoz received the VPI Speed Up Photonics Award in 2002 for innovative Fourier optics AWG with multimode interference (MMI) couplers modeling. He also was granted the IEEE/ Lasers & Electro-Optics Society (LEOS) Graduate Student Fellowship Program in 2002.

Daniel Pastor (S'95–A'97–M'03) was born in Elda, Spain, on November 5, 1969. He received the Ingeniero de Telecomunicacion degree and the Doctor Ingeniero de Telecomunicacion (Ph.D.) degree from the Universidad Politécnica de Valencia (UPV), Valencia, Spain, in 1993 and 1996, respectively.

He joined the Optical Communications Group of the Departamento de Comunicaciones at UPV in 1993, where he was a Lecturer at the Telecommunications Engineering Faculty from 1994 to 1998 and an Associate Professor in 1999. He has published more than 45 papers and conference contributions in the fields of optical delay line filters, fiber Bragg gratings (FBGs), microwave photonics, wavelength-division-multiplexing (WDM), and subcarrier multiplexing lightwave systems. His current technical interests include microwave photonics, FBG applications, and WDM networks.

José Capmany (S'88–M'91–SM'96) was born in Madrid, Spain, on December 15, 1962. He received the Ingeniero de Telecomunicación degree and the Ph.D. degree from the Universidad Politécnica de Madrid, Madrid, Spain, in 1987 and 1991, respectively.

He worked as a Research Assistant at the Departamento de Tecnología Fotónica, Universidad Politécnica de Madrid, from 1988 to 1991. In 1991, he moved to the Departamento de Comunicaciones, Universidad Politécnica de Valencia, Valencia, Spain, where he started the activities on optical communications and photonics, founding the Optical Communications Group (www.gco.upv.es). He was an Associate Professor from 1992 to 1996 and has been a Full Professor in optical communications, systems, and networks since 1996. In parallel, he has been Telecommunications Engineering Faculty Vicedean from 1991 to 1996 and deputy head of the Communications Department since 1996. He is a Member of the Editorial Board of *Fiber and Integrated Optics*, *Microwave and Optical Technology Letters*, and the *International Journal of Optoelectronics*. His research activities and interests cover a wide range of subjects related to optical communications, including optical signal processing, fiber resonators, fiber gratings, radio-frequency filters, subcarrier multiplexing, wavelength-division multiplexing and code-division multiple-access transmission, wavelength conversion, and optical bistability. He has published more than 200 papers in international refereed journals and conferences.

Prof. Capmany has been a Member of the Technical Program Committees of the European Conference on Optical Communications (ECOC), the Optical Fiber Conference (OFC), the Integrated Optics and Optical Communications Conference (IOOC), the Conference on Lasers and Electro-Optics (CLEO) Europe, and the Optoelectronics and Communications Conference (OECC). He has also conducted activities related to professional bodies and is the Founder and current Chairman of the Lasers & Electro-Optics Society (LEOS) Spanish Chapter and a Fellow of the Institution of Electrical Engineers (IEE) and the Optical Society of America (OSA). He received the extraordinary doctorate prize of the Universidad Politécnica de Madrid in 1992.

Daniel Ortega received the B.Eng. degree (first-class) in optoelectronics and lasers from Hull University, Hull, U.K., in 1994 and the Ph.D. degree from the University of Glasgow, Glasgow, U.K., in 1998, where his research investigated the propagation of light in periodic segmented waveguides (PSWs) fabricated in Ti:$LiNbO_3$.

He subsequently worked as a Postdoctoral Researcher in the bioelectronics group at the University of Glasgow from 1998 to 2000, where he investigated optical actuators used to detect fluorescence from DNA assays, using free-space optics and integrated optics. From 2000 to 2003, he worked for Kymata, Ltd., Livingston, U.K. (acquired by Alcatel in 2001). He was responsible for the technical strategy used in the development of arrayed-waveguide gratings, splitters, and interleavers. He was also responsible for the development of new products.

Antoine Pujol received the Ingenieur degree from the Physics Department of INSA Toulouse, Toulouse, France, and the M.Sc. degree in optoelectronics from the University of Essex, Essex, U.K., in 2000.

He then joined Kymata, Ltd., Livingston, U.K. (acquired by Alcatel in 2001), where he contributed to the research and development of planar optics. He was particularly responsible for device characterization and for the development of arrayed-waveguide grating products.

Jim R. Bonar received the Ph.D. degree from the University of Glasgow, Glasgow, U.K., in 1995.

He subsequently became a Research Associate and then a Lecturer at the University of Glasgow. In 1998, he joined the start-up company Kymata, Ltd., Livingston, U.K. (acquired by Alcatel in 2001), which develops and manufactures passive optical components. Since joining the company, he worked as Technology Manager, Product Manager, and R&D Chief Process Engineer. He then became Director of Product Technology for Alcatel Optronics UK, Ltd., and is now Systems Manager for Avanex UK, Ltd., Livingston, U.K. During his career, he has worked on rare-earth-doped silica waveguide amplifiers and lasers, polymer waveguides, multimode structures for sensing applications, and Si micromachining. He has authored and coauthored seven patent applications and more than 30 journal and conference papers.

Dr. Bonar was awarded a Fellowship from the Royal Society of Edinburgh/SE in 1997.